P1.57

NUMERICAL SIMULATION OF MAMMATUS-LIKE CLOUDS IN CIRRUS OUTFLOW ANVILS

Katharine M. Kanak[1], Jerry M. Straka* [2], and David M. Schultz[13]

[1]Cooperative Institute for Mesoscale Meteorological Studies (CIMMS), University of Oklahoma, Norman, OK
[2]School of Meteorology, University of Oklahoma, Norman, OK
[3]National Severe Storms Laboratory, Norman, OK

1. INTRODUCTION

Mammatus clouds are defined as "hanging protuberances, like pouches, on the undersurface of a cloud. This supplementary cloud feature occurs mostly with cirrus, cirrocumulus, altocumulus, altostratus, stratocumulus and cumulonimbus; in the case of cumulonimbus, mamma generally appear on the underside of the anvil." (Glossary of Meteorology, 2000). A distinguishing characteristic of mammatus clouds is their very smooth laminar appearance. A comprehensive review of observations and proposed formation mechanisms of mammatus clouds is given in Schultz et al. (2006).

Winstead et al. (2001) present radar observations that suggest the mammatus are organized into rows that may be perpendicular to the mean wind direction at a given height, although they admit that this orientation may be subjectively chosen. However, if the mammatus are indeed organized into rows perpendicular to a local mean shear vector, this may imply that shear effects are dominating buoyancy effects (as shown by Asai 1970 and others for convection rolls in shear).

At other times, mammatus may appear to have no organized pattern and form in clusters of unequal sized cells (Ludlam and Scorer 1953). Often they appear on the sloping underside (10-15˚ from horizontal plane) of thunderstorm anvils and have been observed on both the upshear and downshear sides of the outflow anvil.

* *Corresponding author address:* Jerry M. Straka, School of Meteorology, University of Oklahoma, Norman, OK, 73019; email: jmstraka@cox.net.

Depending on the height of the anvil outflow (reported at 1400 m by Hlad 1944 and at 7 km by Stith 1995 and Winstead et al. 2001) and the ambient stratification, mammatus may be composed of mostly ice (Stith 1995) mostly liquid (Warner 1973), or a combination of both. Some have proposed that ice composition may explain the laminar appearance, but the existence of mammatus with smooth surfaces at temperatures well above freezing suggest this is not always so.

It should also be pointed out that downward convective motions that resemble mammatus, or a variation of mammatus-type clouds, have also been observed in the absence of deep convective events (e.g. Hlad 1944). Hlad presents a case where mammatus were associated with high-altitude cirrus clouds initiated by the passage of an upper-level disturbance. Scorer (1972) also states that mammatus can occur on falling rain or snow below a cloud base or on streaks of falling ice crystals. Therefore, the altitude at which mammatus formation occur can vary greatly.

Mammatus are most often visible near sunset and sunrise, most likely due to adequate illumination of the underside of clouds that can only occur when the sun angle is very low. This prevalence near sunset/sunrise may suggest that radiation processes may play some role in mammatus formation. The duration of a "field" of mammatus clouds can range from on the order of 15 minutes to as much a few hours. The lifecycle of an individual mammatus cell is much shorter; on the order of 10 minutes (Warner 1973). Physical dimensions of individual mammatus cells have been observed to range

from 250 m (Clarke 1962) to 3 km (e.g., Winstead et al. 2001) in horizontal extent.

There are significant differences reported in the literature on the vertical extent of mammatus cells. Some state the vertical and horizontal scales of motion within mammatus to be nearly equal (Warner 1973). However, some investigators have suggested or provided evidence that mammatus cells may be linked to vertical motions of much greater depth, perhaps even extending from the top of the cirrus outflow anvil to the bottom cloud base of the mammatus cells (e.g., Clarke 1962, Martner 1995). Similarly, the measured magnitude of vertical motions within mammatus varies widely in the observational literature. This may account for the disagreement as to whether or not mammatus are turbulent entities. Reported observed vertical velocities range from -6 m s^{-1} (Kollias et al. 2005) to +3 m s^{-1} Stith (1995). Some recent observations of cirrus clouds using lidar include documentation of mammatus as well (Wang and Sassen 2006). Some examples of observational data from mammatus are given in Table 1.

Study	Vertical Velocity (m s^{-1})	Horizontal Extent (km)
Clarke (1962)	n/a	0.25-0.75
Stith (1995)	-2.5 to +1.0	2-3
Warner (1973)	-3.1 to -1.2	0.1-1
Martner (1995)	-3.0 to +0.5	1.1
Winstead et al. (2001)	-3 to -2	1-3
Kollias et al. (2005)	-6 to +1.5	1-3

Table 1. Some examples of observed physical characteristics of mammatus.

To the authors' knowledge, the only numerical study focused specifically on mammatus that has yet been reported in the literature is by Kanak and Straka (2006).

Many theories of mammatus formation have been proposed. Ludlam and Scorer (1953) were perhaps one of the first to present a theory for the formation of mammatus clouds. When moist cloudy anvil air rapidly flows horizontally over a layer of unsaturated air a vertical moisture gradient exists. As the two layers of air subside, the cloudy layer warms at the moist adiabatic lapse rate, while the unsaturated air below it warms at the dry adiabatic lapse rate. This results in more rapid warming below, less rapid warming above, and a consequent steepening of the local lapse rate. This decrease in static stability can then lead to overturning and vertical convection at the base of the anvil (the cloudy-clear air interface).

Emanuel (1981), in his analytical paper on penetrative downdrafts, suggested that an instability at the cloud base might explain mammatus. His explanation for mammatus is based on mixing similarity theory, and is called cloud base detrainment instability (CBDI). This theory has its origins from cloud top entrainment instability except applied as detrainment at anvil base. In hydrometeor fallout precipitation particles are introduced into a dry sub-layer by vertical flux. In CDBI, however, hydrometeors are introduced into a dry sub-layer by spontaneous mixing under the condition that moist static energy decreases as height increases. The remainder of this discussion of CDBI will be presented in the context of the application of this instability to the current problem which includes precipitation. As pointed out in Emanuel (1981), CBDI typically occurs when potentially cool, saturated air is advected above potentially warm, dry air. This cooler air may be nearly saturated with precipitation in it. This situation is often found in association with thunderstorm anvils, as well as various other clouds systems. To make use of this theory, a condition must be met for CBDI that can be best expressed physically as the liquid-water or ice-water static energy of potentially warm, dry sub-cloud air having greater value than the cloudy-precipitation laden air above.

Martner (1995) presents 8.7 mm radar data taken from a vertically pointing radar that sampled an anvil outflow that exhibited scalloped mammatus-type features. Although, there is no visual confirmation that the data is taken from mammatus (these occurred at night), the 8.7 mm radar typically outlines the shapes of clouds very accurately and is therefore considered to be reliable in its indication of mammatus features. One interpretation of the data is that there are two scales of vertical

motions (Fig. 3b of Martner 1995). One is a deeper scale that is nearly as deep at the anvil cloud depth, and contains alternating upward and downward vertical motions on the order of ±10 m s^{-1}. The second scale of vertical motion is much smaller and occurs in the vicinity of the scalloped cloud base, again with alternating upward and downward vertical motions, but on the order of 1-3 m s^{-1}. This evidence of deeper scale motions lends support for the ideas of Clarke (1962) who proposed gravity waves were a mammatus forcing mechanisms.

The effects of ambient winds and wind shears may possibly contribute to the organization of mammatus cells into rows. Clarke (1962) speculated that Kelvin-Helmholtz (KH) instability (and thus, a Richardson number less than one-quarter), might be a requirement for the existence of mammatus. KH-type patterns have been observed at the bottoms of mammatus cells (Stith 1995, his Fig. 2). Clarke states that this idea was originally put forth by Berg (1938). He also states that wind shear can act to enhance the cloud base moisture gradient and contribute to any evaporative cooling that may have been produced there by the fallout of larger hydrometeors. Another explanation for the regular planforms of mammatus is that the cloud anvil base is already participating in Benard cell-type convection when larger particles fall into it and mammatus are manifest (Wagner 1948, Clarke 1962, Schaefer and Day 1981).

The purpose of this work is to numerically simulate mammatus-like clouds using observed soundings for the specific environments of cirrus outflow anvils in order to attempt to better understand what dynamical or microphysical processes may be responsible for their formation. Because of the scarcity of mammatus observations, numerical simulations provide an attractive methodology to evaluate some of these proposed mechanisms.

2. METHODOLOGY

2.1. Numerical model description

The numerical model used for the experiments is the SAM (Straka Atmospheric Model), a three-dimensional, fully compressible, nonhydrostatic model. The model equations are presented in Carpenter et al. (1998). The velocity fields are advected with a sixth-order local spectral scheme (Straka and Anderson 1993). Divergence and the pressure gradient are solved using sixth-order centered spatial differences. Finally the scalars are advected with a sixth-order Crowley flux scheme (Trembeck et al. 1987) with a flux limiter (Leonard 1991). The sub-grid turbulence closure is a 1.5-order scheme (Deardorff 1980) which also employs a sixth-order spatial discretization. The integration of the fast and slow solution modes are split from each other with the centered-in-time leapfrog scheme used for the slow modes, and an explicit forward-backward solver for the pressure gradient in the velocity equations and mass flux divergence in the pressure equation. Periodic lateral boundary conditions are used. At the upper and lower boundaries, the vertical velocity is equal to zero and the boundaries are specified as free-slip.

The microphysics of the model is described by Straka and Mansell (2005) and for the present study utilizes a single-moment scheme that predicts mixing ratio. Water vapor, snow aggregates, and ice crystal mixing ratios are specified in the initial cirrus anvil cloud. There are numerous other larger ice categories available in the model, but the processes that activate them do not occur in this simulation. The microphysical processes that are represented for the conditions of these simulations include sublimation and deposition of ice and snow aggregates, along with aggregation of ice crystals into snow aggregates. As there is no available cloud water in the simulation domain, there is no riming and thus, no graupel or other rimed ice particles form.

2.2. Numerical experiment designs

A suite of numerical simulations using different observed soundings has been carried out to simulate mammatus-like clouds associated with cirrus outflow anvils. The model domain is intended to represent a roughly rectangular portion of a thunderstorm cirrus outflow anvil at some distance downwind of the main thunderstorm updraft, as mammatus are often observed to be located at great distances from the main thunderstorm, for example, Stith 1995 reports mammatus located 70 km from the

main storm updraft (see his Fig. 1b).

The model domain is 4000 m x 4000 m x 6000 m with 50 m grid spacing in all directions (80 x 80 x 120 grid points). The domain extends from 3500 m above ground level (AGL) to 9500 m AGL in the vertical in all but one simulation, where the domain extends from 3000 m AGL to 9000 m AGL. A time step of 1 s can be used for the slow modes, while the small time step is 0.04 s is used for the fast modes to ensure numerical stability.

The initial conditions are horizontally homogeneous and mean potential temperature and mean dewpoint are specified using observed sounding thermodynamic data (Fig. 1). No mean winds are prescribed in these simulations. The model is initialized by specifying a constant ice crystal mixing ratio, between 8500 m and 9500 m (and 8000 m to 9000 m for the one simulation), of 1.00 x 10^{-3} Kg Kg^{-1}, which is consistent with the values observed by Heymsfield and Knollenberg (1972) and Stith (1995). Then random perturbations of ice crystal mixing ratio of $\pm$ 0.25 x 10^{-3} Kg Kg^{-1} are added at the initial time step in this layer. In addition 7.5 x 10^{-4} Kg Kg^{-1} of snow aggregate mixing ratio is specified in the same layer with random perturbations snow aggregate mixing ratio of $\pm$ 0.25 x 10^{-3} Kg Kg^{-1} added.

3. RESULTS

3.1 Observed soundings

Simulations were conducted using mammatus proximity soundings, and one simulation was made using a sounding that passed through a thick anvil but exhibited no observed mammatus. The portions of the observed soundings that correspond to the simulation domains are shown in the black curves of Figs. 1a-f. Sensitivity of the simulated mammatus to changes in sublimation and fallout, are made using the sounding from Fig. 1b. The red lines represent the thermodynamic profiles taken at the later times in each simulation as denoted in Table 2. These sets of experiments and times are summarized in Table 2.

Expt	Date	Description/ Results	XZ Time (min)
S1	19 Sep 02 00 UTC	mammatus	26
S2	21 May 01 00 UTC	mammatus	30
S3	01 Sep 01 00 UTC	mammatus	33
S4	25 May 04 00 UTC	mammatus	36
S5	04 Sep 01 00 UTC	No mamm	34
S6	04 08 04 12 UTC	No mamm	30
f2	05 21 01 00 UTC	No Sublim	30
s2	05 21 01 00 UTC	No Fall-out	20

Table 2. Summary of numerical experiment names, dates of observed soundings used to initialize the simulations, results and/or description of the simulations, and the times selected for further examination in each case.

All the soundings were taken from Norman, Oklahoma. In cases S1-S5, mammatus clouds were observed visually to be occurring, at or near, the time of the sounding, at a location approximately 5 km from the sounding release point. Mammatus visually were observed on 18 Sept 02 from 2330 UTC to 19 Sept 02 0030 UTC for case S1. Mammatus were observed 21 May 2001 at 2351 UTC for case S2. The exact time of the visual observation of mammatus for S3 unfortunately was not recorded. Mammatus were observed from about 2310 UTC 23 May 2004 to 0000 UTC on 24 May 2004 for case S4. For the case S5, mammatus were observed from 2030 UTC to 2115 UTC on 04 Sept. 2001. Therefore for case S5, the visually observed mammatus occurred quite a while before the sounding was released. This could account for the fact that no mammatus formed in the simulation using the S5 sounding, since it may not have been representative of a mammatus environment. Case S6 represents the case in which an anvil cloud was visible but mammatus were not detected. Thus, mammatus were not expected to form in the simulation initialized using this sounding and this indeed turned out to be the case.

Each initial sounding is shown in Fig. 1 in black lines. The leftmost line represents the dewpoint and the rightmost line represents the temperature. The red lines denote the average thermodynamic profiles and wind vectors at the later simulation time selected for further study for each simulation (last column of Table 2). Experiments f2 and s2 are the two sensitivity experiments to assess the relative importance of sublimation and fallout to the formation of the

mammatus clouds. For these simulations the sounding from case S2 (black curves in Figs. 1g-h) was used. In case f2 (s2), the sublimation (fallout of hydrometeors) process was "turned off" and no sublimation (no fallout) was allowed to occur in the simulation. Mammatus type lobes formed in the s2 case but not in the f2 case.

Some of the main differences between the initial soundings, S1-S6, include the depth of the dry layer just below the likely cloud base (Fig.1a vs. 1b vs. 1c), the presence or absence of an inversion at the anvil base (Fig. 1b,c, e, and f vs. 1d) and the overall degree of static instability in each case. Soundings presented in Winstead et al. (2001), Stith (1995) and Clarke (1962) show proximity soundings with shallow inversions which are possibly associated with cloud bases and/or mammatus.

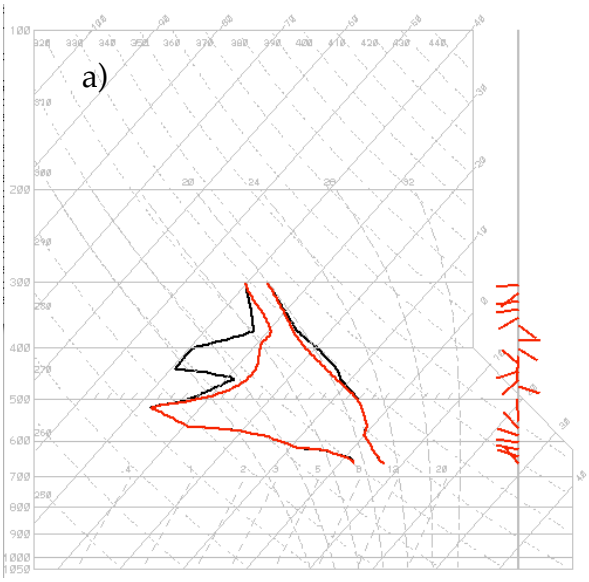

Figure 1. Portions of observed soundings (black lines) that were used in the initialization of the numerical simulations. Dewpoint (left hand side lines) and temperature (right hand side lines) are plotted. Also shown (red) is the profile of the horizontal mean perturbation potential temperature added to the base state at the selected later times shown in Table 1. Red wind vectors from the simulations are also plotted. a) Experiment S1 at time t = 0 (black) and time t = 26 min (red). The vertical domain extends from 3500 m to 9500 m.

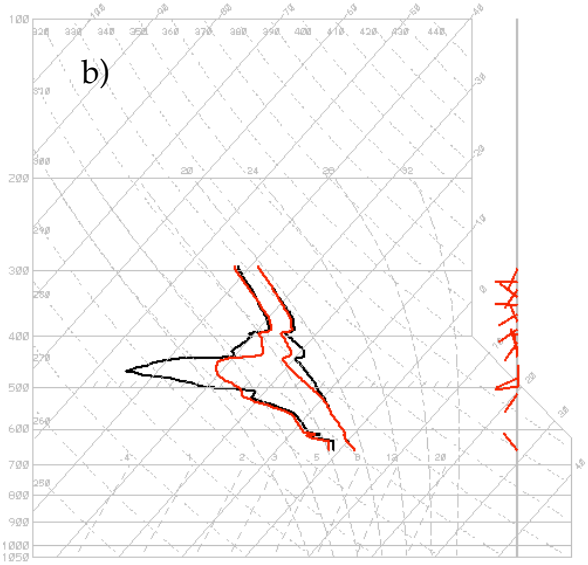

Figure 1. Cont. b) Experiment S2, at time t = 0 (black) and time t = 30 min (red). The vertical domain extends from 3500 m to 9500 m.

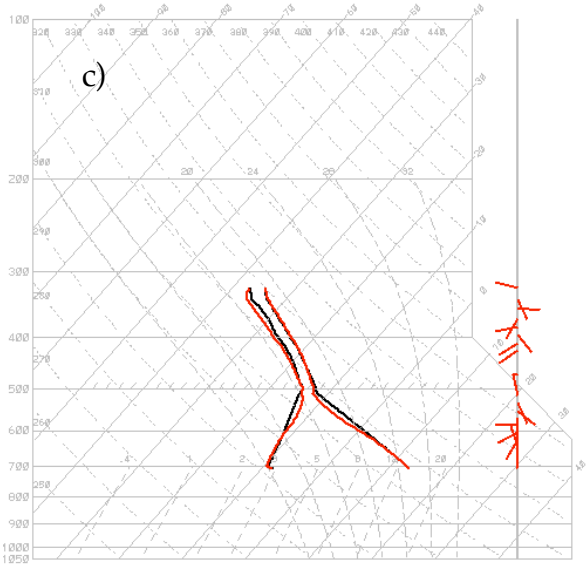

Figure 1. Cont. c) Experiment S3 at time t = 0 (black) and time t = 33 min (red). The vertical domain extends from 3500 m to 9500 m.

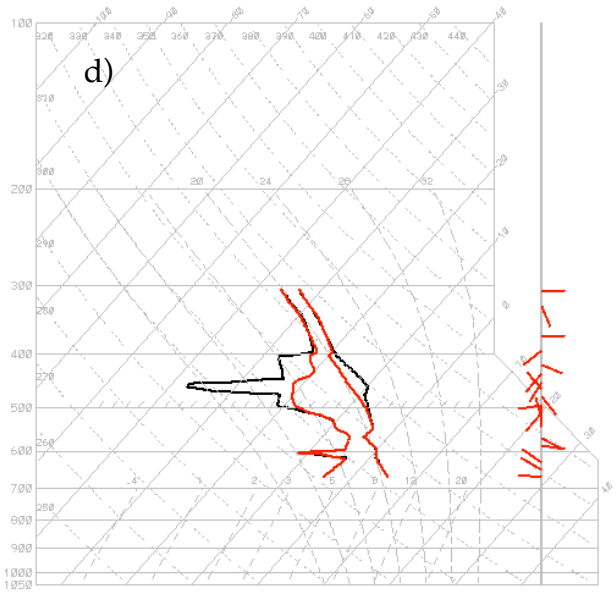

Figure 1. Cont. d) Experiment S4 at time t = 0 (black) and time t = 36 min (red). The vertical domain extends from 3000 m to 9000 m.

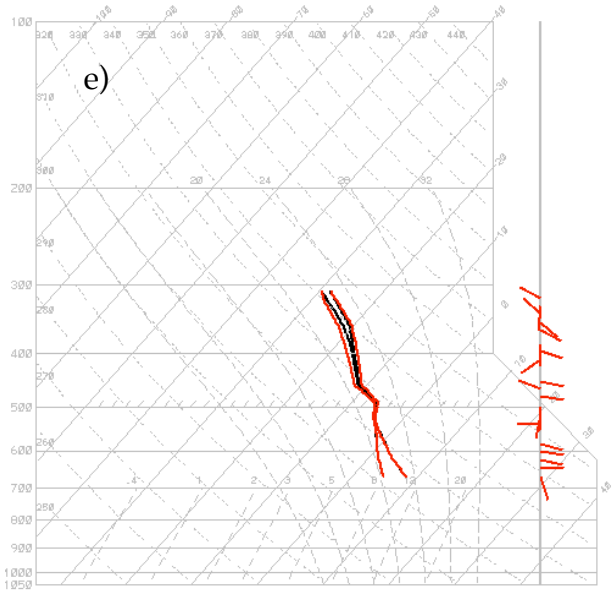

Figure 1. Cont. e) Experiment S5 at time t = 0 (black) and time t = 34 min (red). The vertical domain extends from 3500 m to 9500 m.

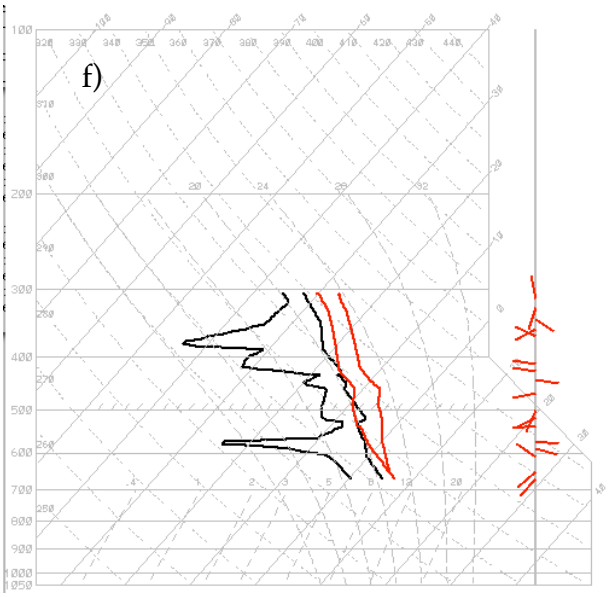

Figure 1. Cont. f) Experiment S6 at time t = 0 (black) and time t = 30 min (red). The vertical domain extends from 3500 m to 9500 m.

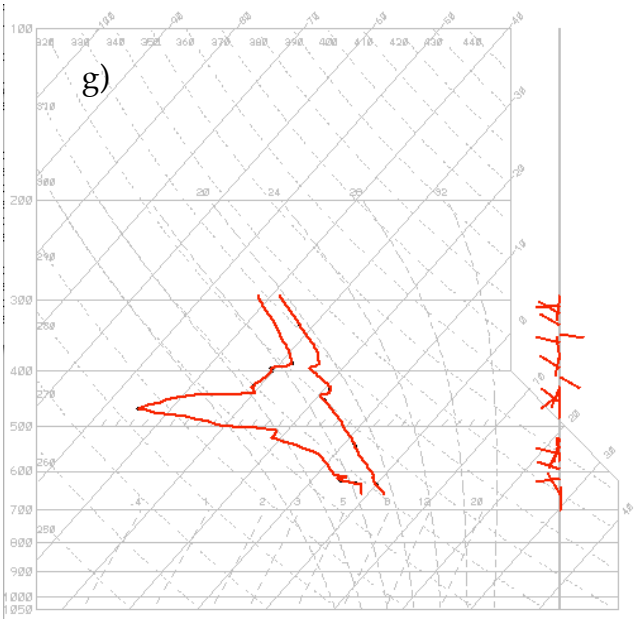

Figure 1. Cont. g) Experiment f2 at time t = 0 (black) and time t = 30 min (red). The vertical domain extends from 3500 m to 9500 m.

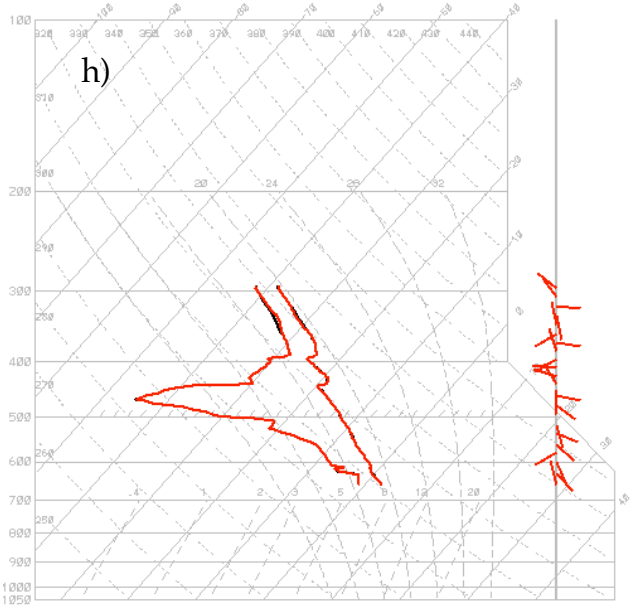

Figure 1. Cont. h) Experiment s2 at time t = 0 (black) and time t = 20 min (red). The vertical domain extends from 3500 m to 9500 m.

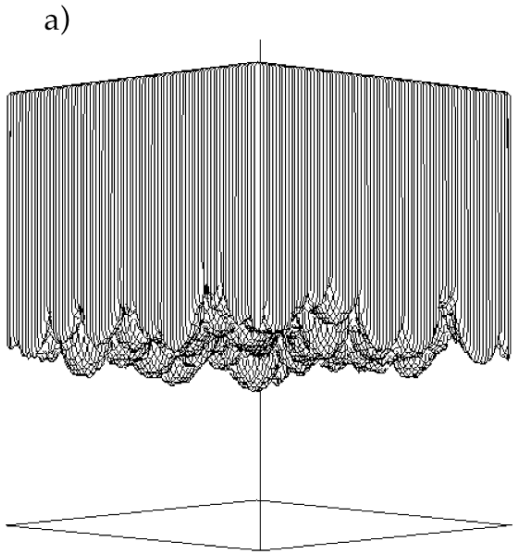

Figure 2. Three-dimensional isosurface of 1 x 10^{-5} m of snow diameter. a) Experiment S1 at time t = 26 s.

3.2. Isosurfaces of mammatus-like features

Three-dimensional isosurfaces at various times are shown for the experiments S1, S2, and S3. The isosurface is 1 x 10^{-5} m of snow diameter. The times shown were selected to be times when the mammatus lobes first appear to be mature. These times correspond to the times in Table 2 as well. The lobes of a) and b) appear similar although their time evolution is different and there is a much deeper layer of dry air in the original sounding for S1 than for S2 (Fig. 1a,b). That is, it takes more simulation time in S2 for the mammatus lobes to appear as mature as those in S1. The lobes in c) are much narrower than in a) and b). That is, the horizontal width of the lobes are much smaller in this case, which has the shallowest dry layer of the cases S1-S3. Keep in mind that this is just one isosurface of snow diameter. Mammatus also formed for case S4 but are similar to S1 and S2, and mammatus-like lobes did not form for simulations S5 and S6 and thus, neither of these results are shown here.

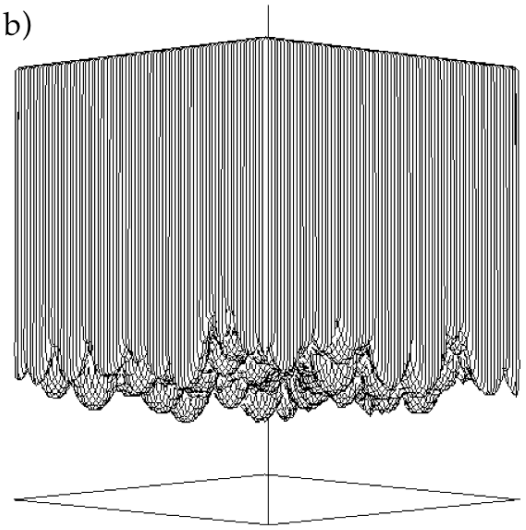

Figure 2. Cont. b) Experiment S2 at time t = 30 s.

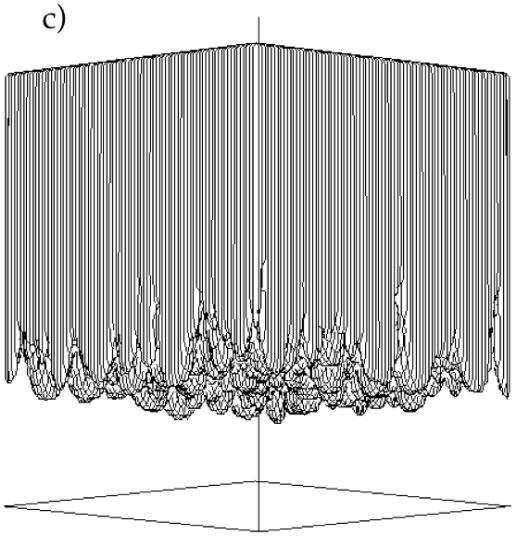

Figure 2. Cont. c) Experiment S3 at time t = 33 s.

3.3. Vertical cross-sections of snow diameter for cases S1-S3

Vertical cross-sections of contours of the of the snow diameter are shown next. The location of the cross-section was chosen as the location of the domain minimum in vertical velocity for each simulation. This location was associated with a mammatus lobe in all of the simulations. The times selected again correspond to the times in Table 2 and in Fig. 2.

Figures 3a-3f show the XZ cross-section of the snow diameter contours. The lowest most contour would correspond to what an observer from the ground would see as mammatus-like clouds bases. Figures 3a,c, and e show the whole domain while Figs. 3b. d, and f show expanded plots of the regions within the black boxes denoted on Figs. 3a, c, and e.

The horizontal extent of the lobes in case S1 (Fig. 3a) is about 400-500 m which is similar to some of those reported in Table 1. Differences may be due to resolution differences in measuring devices and the simulations. Vertical motion within the simulated lobes is about -1 to -3.7 m s^{-1} which is quite similar to the measurements of Stith (1995; Table 1). Fig 3b shows indication of upward return flow within the leftmost mammatus lobe as determined from the wind vectors. This pattern is similar to the pattern shown by Winstead et al. (2001; their Fig 6a).

Figure 3c and d (Case S2) show similar results to those of case S1. Figure 3c shows that there is more space between the mammatus lobes than in Fig. 3a. The lobes are approximately 300-450 m and vertical motion is about -7.6 m s^{-1}. The horizontal extent is similar to some of the observations in Table 1, but is smaller than most observed, while the vertical velocity is amplitude is similar to those in Table 1. Figure 3d shows that there are horizontal rotors above the lobes (left-hand side of the Figure).

Case S3 (Fig.e-f) exhibits mammatus lobes that are much narrower in the horizontal direction than in cases S1 and S2 (Fig.3a-d). That is, the horizontal lobes are about 250 m wide and the vertical velocity is -0.61 m s^{-1}, which is considerably smaller than in S1 and S2. Figure 3f shows that the vertical gradient of snow diameter at the base of each mammatus lobe is weaker than in cases S1 and S2. The reason for these differences is not yet known, but one of the goals of this ongoing study is to seek the mechanism that determines the horizontal extent of these convective lobes. Figure 3f also exhibits horizontal rotors above the lobe bases.

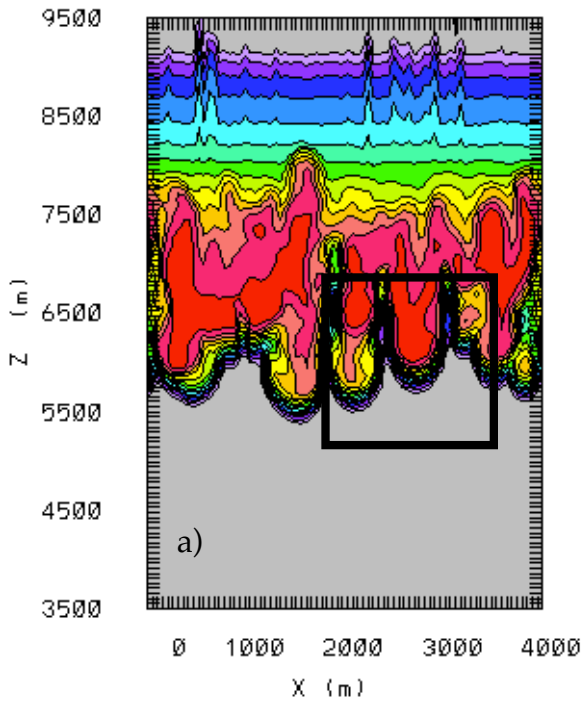

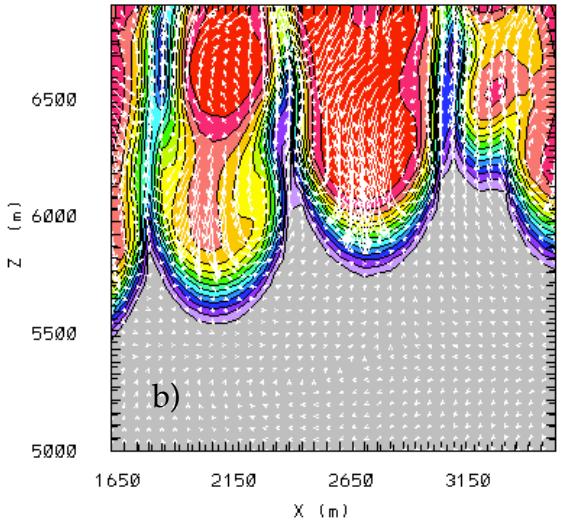

Figure 3. XZ cross-sections of snow diameter contours at t = 26 min, y = 125 m for S1. Minimum value (gray) is 0.0 to maximum value (red) 0.58 mm with interval of 0.04 mm. a) Whole domain. b) Expanded region of Fig. 3a with velocity vectors in white.

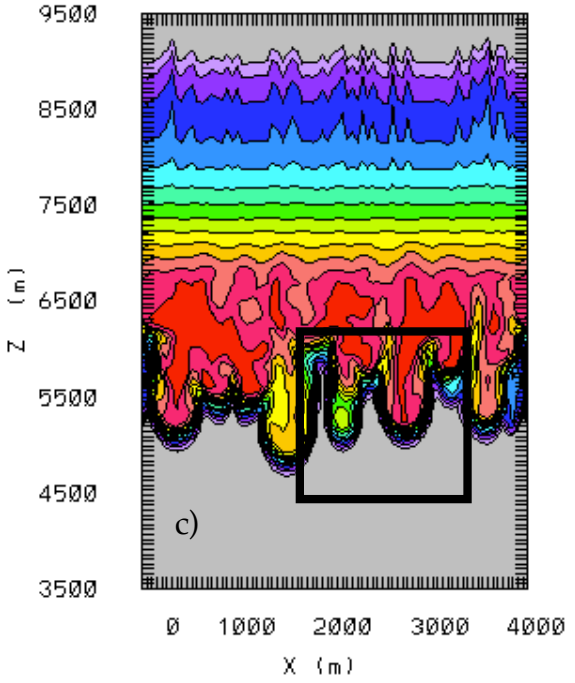

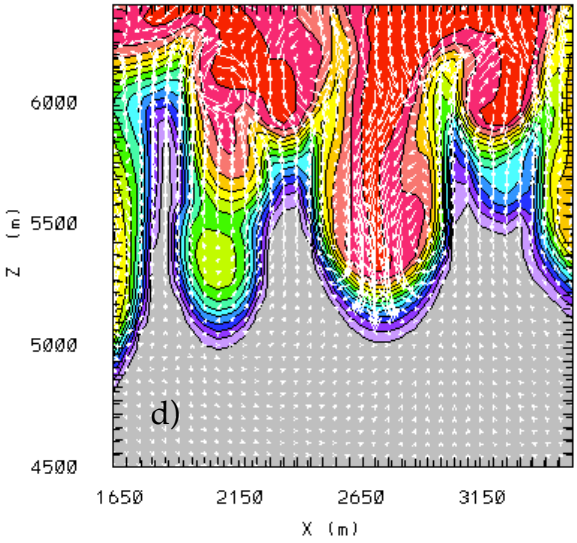

Figure 3. cont. XZ cross-sections of snow diameter contours at t = 30 min, y = 75 m for S2. Minimum value (gray) is 0.0 to maximum value (red) 0.7 mm with interval of 0.05 mm. c) Whole domain. d) Expanded region of Fig. 3c with velocity vectors in white.

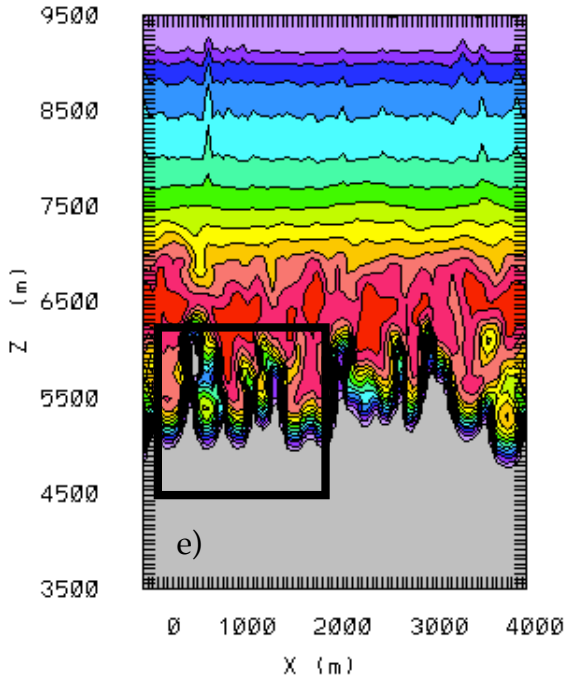

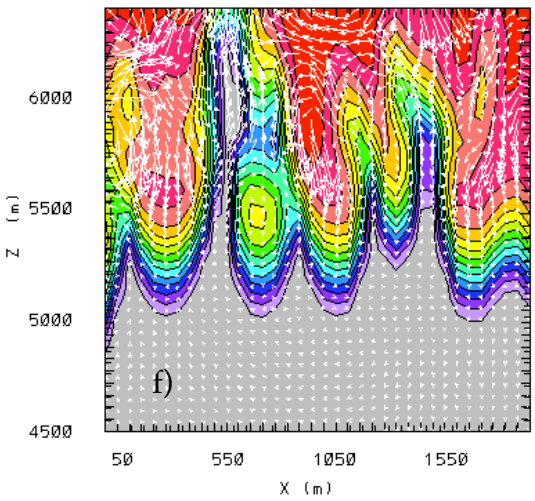

Figure 3. Cont. XZ cross-sections of snow diameter contours at t = 33 min, y = 1625 m for S3. Minimum value (gray) is 0.0 to maximum value (red) 0.55 mm with interval of 0.04 mm. e) Whole domain. f) Expanded region of Fig. 3e with velocity vectors in white.

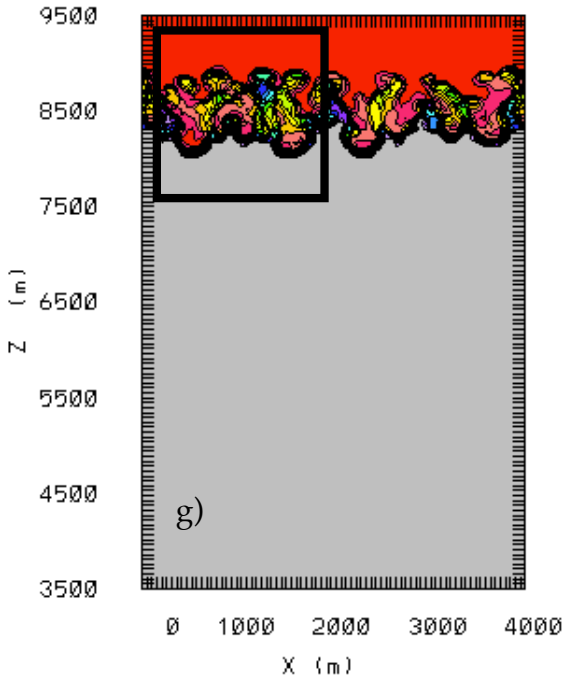

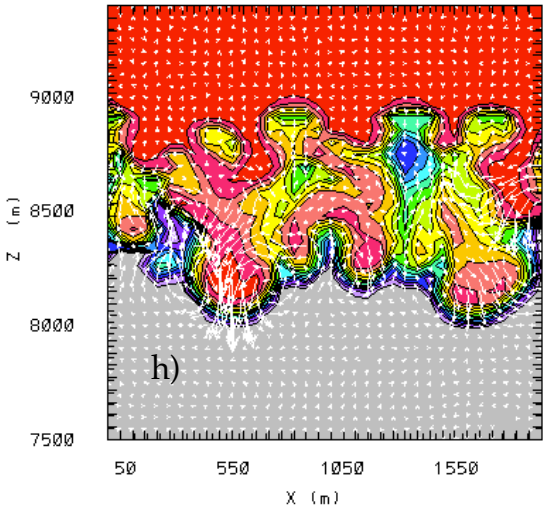

Figure 3. Cont. XZ cross-sections of snow diameter contours at t = 20 min, y = 3725 m for s2. Minimum value (gray) is 0.0 to maximum value (red) 1.0 mm with interval of 0.07 mm. g) Whole domain. h) Expanded region of Fig. 3g with velocity vectors in white.

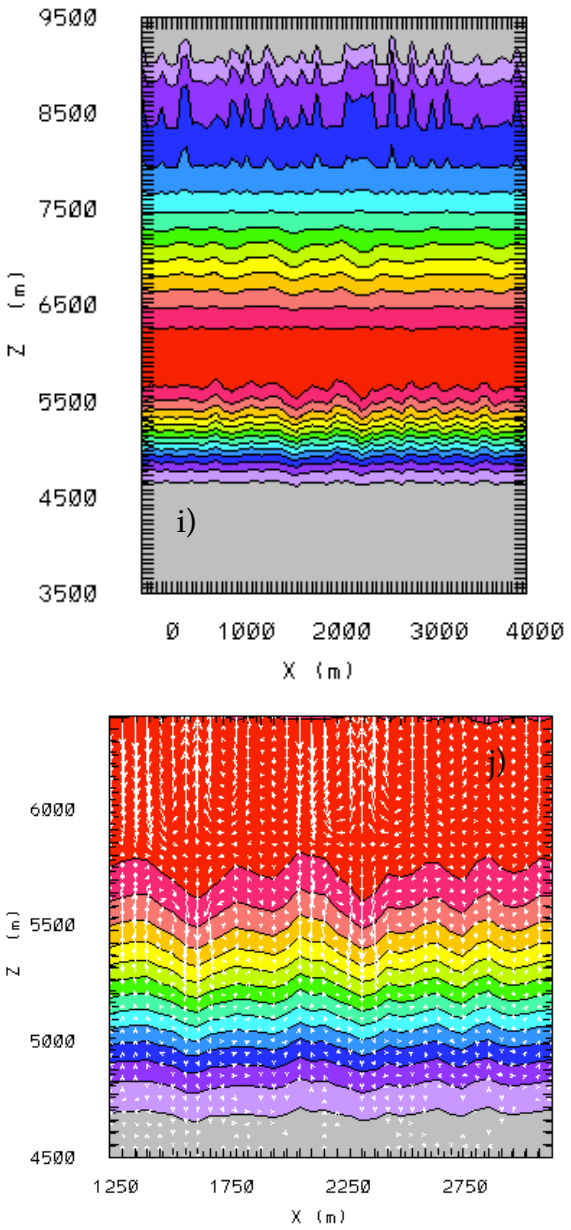

Figure 3. Cont. XZ cross-sections of snow diameter contours at t = 30 min, y = 1675 m for f2. Minimum value (gray) is 0.0 to maximum value (red) 0.9 mm with interval of 0.065 mm. i) Whole domain. j) Expanded region of Fig. 3i with velocity vectors in white.

3.5. Sublimation and Fallout

Figure 3g and h (Case s2) shows the snow diameter for the simulation in which fallout is not allowed to occur in the simulation. Figure 3g shows that lobe type structures still occur but are significantly different than the other cases. The lobes are confined to the upper part of the simulation domain. In addition they are not distinctly separated from one another as in the other cases. The expanded view in Fig. 3h shows that the lobes are about 300-400 m in horizontal extent. The lobe in the left part of Fig. 3h exhibits upward return flow, again similar to that shown by Winstead et al. (2001; their Fig. 6 a). The maximum amplitude of snow diameter is 1.0 mm, which is greater by about a factor of two than the cases previously discussed.

The next case is f2 is the simulation in which sublimation is not allowed to occur, but fallout is permitted. In this case, no mammatus type lobes form (Fig. 3 i-j). These results appear qualitatively similar to cases S5-S6 in which no mammatus lobes form either.

Comparison of cases s2 and f2 show that sublimation may be a necessary condition for mammatus lobes, while fallout appears to result in deeper lobes that may possibly be more consistent with observations of mammatus. In addition, fallout permits deeper motions within the cirrus anvil cloud that could be an important part of mammatus dynamics for some cases. Two examples of observational works that exhibit deeper motions are Martner (1995) and Winstead et al. (2001).

3.6. Temperature

Figure 4 shows, for the expanded portions of the domain, the perturbation potential temperature in color shading with the snow diameter contours overlain in black. It is clear that whether or not the center of a mammatus lobe is considered warmer or colder than ambient depends strongly on the height at which the temperature is evaluated and also possibly on the time in the evolution of a mammatus cloud life cycle. For this case S1, (Fig. 4a) throughout most of the depth of these sampled lobes at this time, the cores have perturbation potential temperatures that are approximately 0.4 K greater than ambient. Stith (1995) states that the center of a mammatus lobe was 0.7 ˚C warmer than ambient temperatures, while other investigators state that the descending mammatus must be colder owing to sublimation and/or evaporative cooling. In the case of S1, the simulation results at this time in the mammatus evolution support the findings of Stith

(1995).

For the case S2, Fig. 4b shows that there are both warmer and colder cores within the center of lobes. Specifically the rightmost lobe has a colder than ambient core while the leftmost lobes of Fig. 4b has warmer potential temperatures near the bottom on the lobe.

Figure 4c shows that for most of the mammatus lobe depth the potential temperature is near ambient. A conclusion that may be drawn from Fig. 4 is that mammatus lobes can have higher or lower perturbation potential temperatures than ambient depending, on life cycle, height within the lobe, or other factors yet to be determined. This could account for the discrepancies in the literature on this issue.

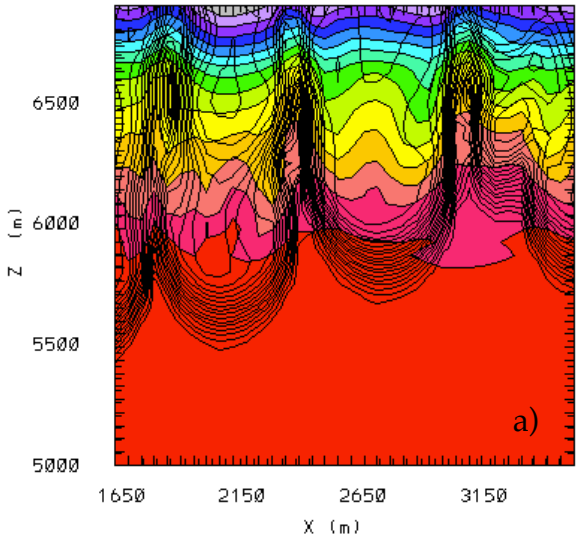

Figure 4. a) XZ cross-sections of black contours of snow diameter at t = 26 min, y = 125 m for S1. Black minimum value is zero mm and the maximum contour is 0.57 mm with an interval of 0.03 mm. Shaded contours are perturbation potential temperature. Minimum value (gray) is -2.51 K to maximum value (red) 0.08 K with interval of 1.1 K.

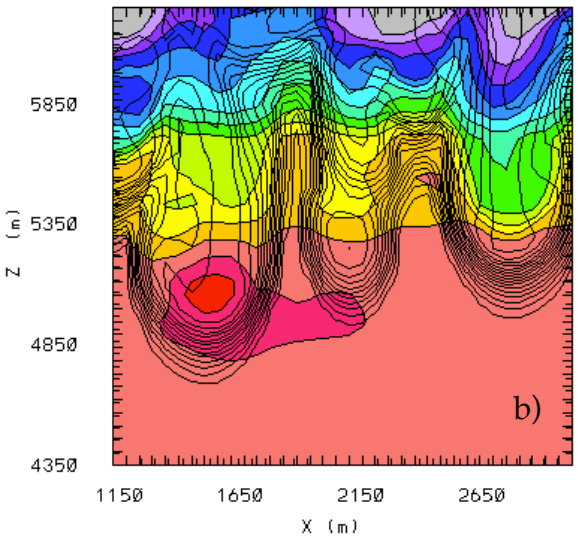

Figure 4. Cont. b) XZ cross-sections of black contours of snow diameter at t = 30 min, y = 75 m for S2. Black minimum value is zero mm and the maximum contour is 0.57 mm with an interval of 0.03 mm. Shaded contours are perturbation potential temperature. Minimum value (gray) is -2.64 K to maximum value (red) 0.476 K with interval of 0.2 K.

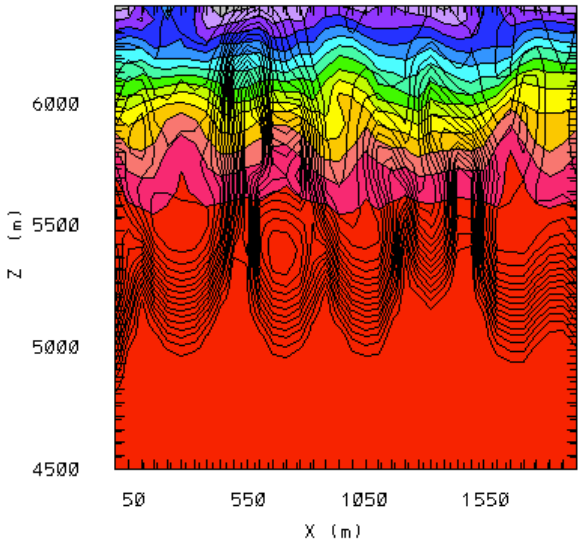

Figure 4. Cont. c) XZ cross-sections of black contours of snow diameter at t = 33 min, y = 1625 m for S3). Black minimum value is zero mm and the maximum contour is 0.54 mm with an interval of 0.03 mm. Shaded perturbation potential temperature. Minimum value (gray) is -1.73 K to maximum value (red) 0.15 K with interval of 0.125 K.

3.7. Time evolutions of XZ plots

In this section, two interesting features that occur late in the simulations are presented. The first is shown in Fig. 5a in which the snow diameter is in color shading and the velocity vectors are overlain in black. This Figure shows a portion of a domain at a time late in the simulation, t = 36 min. The flow has become very turbulent and upon comparison with Fig. 3a (S1 at t = 26 min), it is evident that the cloud field appears to be retreating upward owing to sublimation. Thus, after some time, the mammatus lobes may reach some type of equilibrium level and cease descending.

Figure 5b shows the snow diameter in color and the velocity vectors overlain in black for case S3 at t = 37 min. This Figure can be compared with Fig. 3d which is at t = 30 min. The main feature to be highlighted is that a portion of the snow diameter (which may be used as a proxy for cloud) breaks away from one of the lobes. This is the second lobe from the left side of the Fig. 5b. This process in which portions of mammatus lobe break away from the main lobe has not been reported to have been observed visually from the ground, but could still be occurring. Emanuel's (1981) Fig. 3 suggests such possible behavior as detrainment continues and cloudy air mixes with dry air.

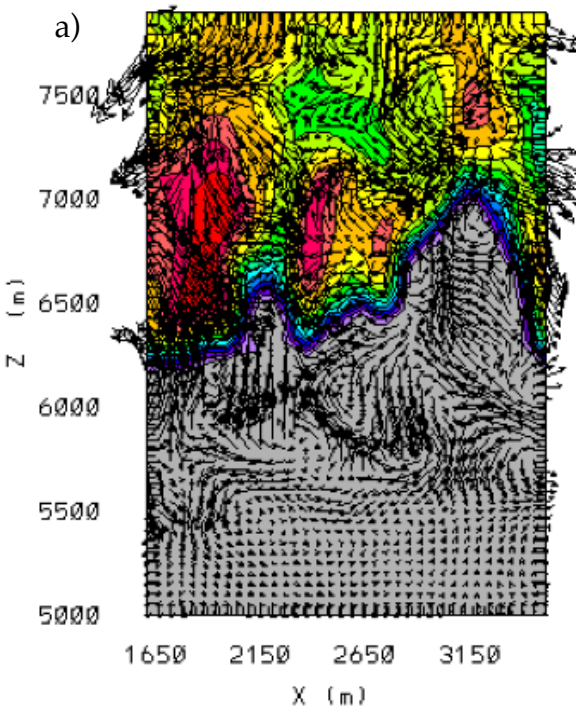

Figure 5. a) XZ cross-section of black velocity vectors and snow diameter (color shading) at t = 36 min, y = 125 m for S1. For snow diameter, the minimum value (gray) is 0.0 mm to maximum value (red) 0.225 mm with interval of 0.016 mm.

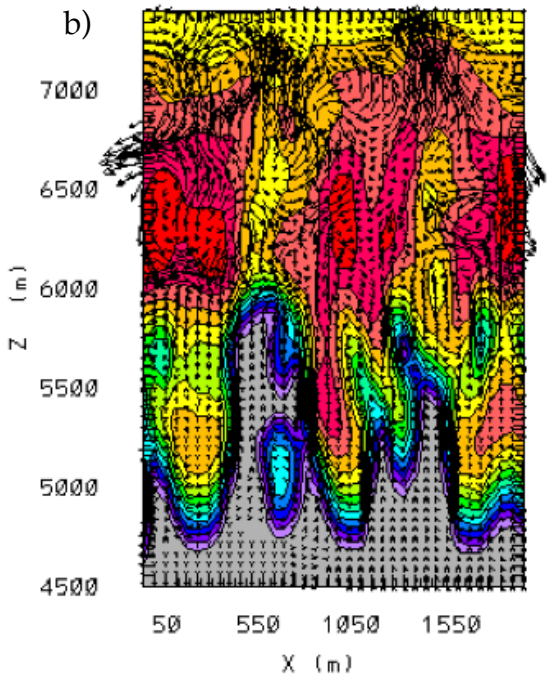

Figure 5 Cont. b) XZ cross-sections of black velocity vectors and snow diameter (color shading) at t = 37 min, y = 1625 m for S3. For snow diameter, the minimum value (gray) is 0.0 mm to maximum value (red) 0.41 mm with interval of 0.03 mm.

3.8 Modification of original soundings by mammatus-like features

In this section, the original soundings and Fig. 1 are revisited to examine the red curves. In Fig. 1 the red lines represent the soundings at the time listed in Table 2 for each simulation. In most cases (Figs. 1a, b, c) the dry layers are mixed and the resulting soundings are more moist after the cloud has passed these levels during the descent of the simulated cloud. An exception is case S4, although this sounding appears quite different from S1-S3 initially, the common feature is that there are dryer layers below what is likely a cloud base.

At this time there is no recognizable pattern mean wind vectors that are plotted in red and the meaning of these winds is unclear. Another intriguing result is the evolution of the soundings for case S5 (Fig. 1e). There were no

mammatus lobes for this case but the evolution of the sounding is dramatic. This was the case in which the mammatus were observed 2-3 hours prior to the sounding collection time. It is possible that the sounding data partially represents a mammatus environment, but not completely enough for them to occur in a simulation initialized using this sounding. However, as in the cases S1-S3 the sounding taken near the end of the simulation has higher overall relative humidity.

3.8. Vertical vortices in simulations

Another interesting finding from the simulations, is the existence of vertical vortices at heights near the approximate cloud base of the parent anvil cloud. Figure 6 shows a vertical cross-section of a portion of the domain of snow diameter contours in color and velocity vectors overlain in black for the case S2 at time t = 30 min. The white line is the location of horizontal cross-section across which Figs. 6b, c, and d are taken. Figure 6b is the horizontal cross section of contours of vertical vorticity. The warm (cool) colors are positive (negative) vorticity values. The pattern shows evidence of many counter-rotating couplets. An expanded version of the black box in Fig. 6b is shown in Fig. 6c with horizontal velocity vectors overlain in white. For clarity Fig. 6d is included to show just the wind vectors. Examination of Fig. 6c and d show that there are several counter-rotating couplets of closed circulations in the velocity vector fields. It may be conjectured that if the simulated mammatus lobes contain large values of negative vorticity (and thus high amplitudes of helicity) they might have enhanced downward motion due to inhibition of lateral mixing. However, this is strictly speculation at this point.

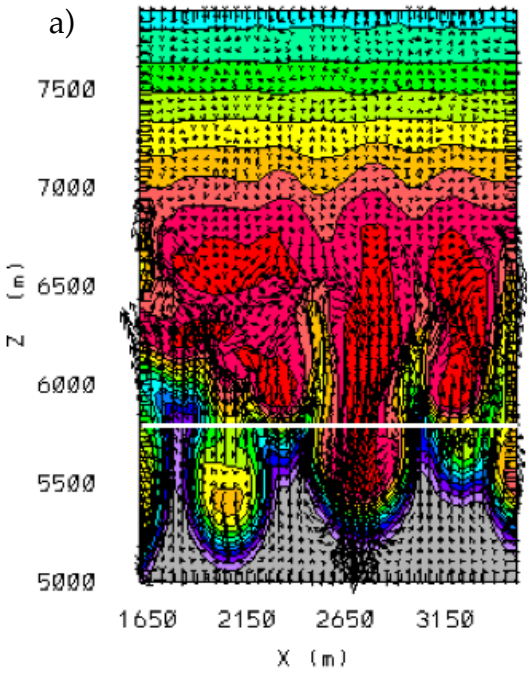

Figure 6. a) XZ cross-sections of black velocity vectors and snow diameter (color shading) at t = 30 min, y = 75 m for S2. Minimum value (gray) is 0.0 mm to maximum value (red) 0.73 mm with interval of 0.05 mm.

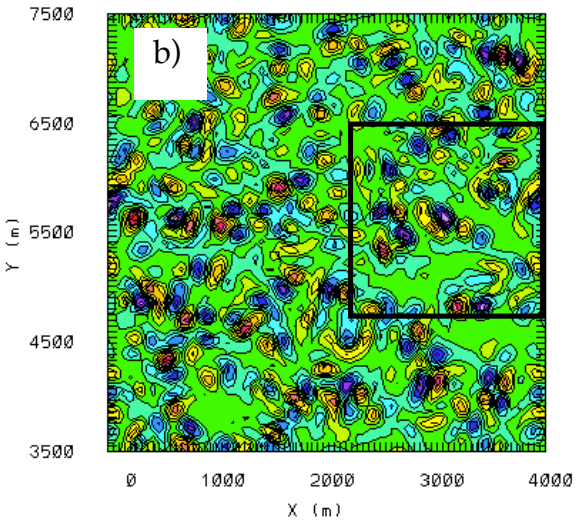

Figure 6. Cont. b) XY cross section of vertical vorticity taken at white line in Fig. 6a at t = 30 min, z = 5775 m. Full domain. Minimum value is -0.053 s^{-1} (grey) and maximum value as 0.05 s^{-1} (red). Interval is 0.01 s^{-1}.

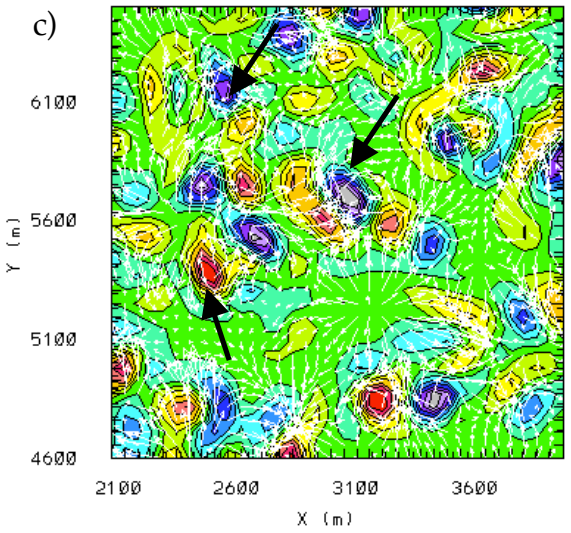

Figure 6. Cont. c) Expanded region of black box in Fig. 6b with horizontal velocity vectors overlain in white. Minimum value is -0.044 s^{-1} (grey) and maximum value as 0.04 s^{-1} (red). Interval is 0.006 s^{-1}.

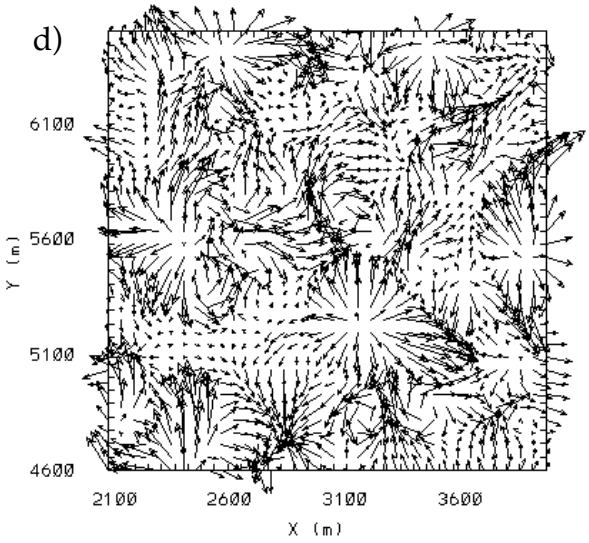

Figure 6. Cont. d) Expanded region of black box in Fig. 6b. Horizontal velocity vectors that display vertical vortices.

4. SUMMARY

In this paper, it has been demonstrated that mammatus-like clouds can be numerically simulated using high resolution experimental designs. Observed soundings that were close in time and space to visual observations of mammatus clouds were used to initialize the simulations. The simulated mammatus clouds exhibited rounded, pouch-like protuberances at the base of a layer of cloud ice and snow with physical dimensions and vertical motions that were similar to actual observations of mammatus clouds.

Two experiments were conducted to examine the relative effects of fallout of hydrometeors and sublimation of ice. It was found that no mammatus formed when sublimation was not allowed to occur and although mammatus lobes formed when fallout was not allowed to occur, the character of these lobes was quite different from the other simulations. Explanations for these results are still being sought.

Examination of the potential temperature fields showed that the mammatus lobes may have either warmer or colder cores than ambient depending on the height within the mammatus lobe and possibly also on the stage of a mammatus cloud's lifecycle.

The resulting soundings at later times in the simulations, after the mammatus had formed, included a general moistening of the original dry layers. This could be due to mixing or the dynamics of the mammatus clouds or other yet unknown mechanisms.

Future work will include further attempts to evaluate proposed formation mechanisms and further sensitivity experiments.

Acknowledgments: The authors are grateful to Dr. Kerry Emanuel for many helpful suggestions and discussions.

5. REFERENCES

Asai, T., 1970: Three-dimensional features of thermal convection in a plane Couette flow. *J. Meteor. Soc. Japan*, **48**, 18-29.

Berg, H. 1938: *Met. Zeit.*, **55**, p.283.

Carpenter, R. L., Droegemeier K. K., and A. M. Blyth, 1998: Entrainment and detrainment in numerically simulated cumulus congestus clouds. Part I: General results. *J. Atmos. Sci.*, **55**, 3417–3432.

Clarke, R. H., 1962: Pressure oscillations and fallout downdraughts. *Quart. J. Roy. Meteor. Soc.*, **88**, 459-469.

Deardorff, J. W., 1980: Stratocumulus-capped mixed layers derived from a three-dimensional model. *Bound.-Layer Meteor.,* **18**, 495–527.

Emanuel, K. A., 1981: A similarity theory for unsaturated downdrafts within clouds. *J. Atmos. Sci.*, **38**, 1541–1557.

Glossary of Meteorology, Second Edition, 2000. T. S. Glickman, Editor. American Meteorological Society, Boston, MA.

Heymsfield, A. J. and R. G. Knollenberg, 1972: Properties of cirrus generating cells. *J. Atmos. Sci.*, **29**, 1358–1366.

Hlad, C. J., Jr., 1944: Stability tendency and mammatocumulus clouds. *Bull. Amer. Meteor. Soc.*, **25**, 327–331.

Kanak, K. M. and J. M. Straka, 2006: An idealized numerical simulation of mammatus-like clouds. *Atmospheric Science Letters*, **7(1)**, 2-8. DOI: 10.1002/asl.121

Kollias, P., I. Jo, and B. A. Albrecht, 2005: High-resolution observations of mammatus in tropical anvils. *Mon. Wea. Rev.*, **133,** 2105-2112.

Leonard, B. P., 1991: The ULTIMATE conservative difference scheme applied to unsteady one-dimensional advection. *Computational Methods in Applied Mechanics and Engineering*, **88**, 17-74.

Ludlum, F. H., and R. S. Scorer, 1953: Convection in the atmosphere. *Quart. J. Roy. Meteor. Soc.*, **79**, 317-341.

Martner, B. E., 1995: Doppler radar observations of mammatus. *Mon. Wea. Rev.*, **123**, 3115–3121.

Schaefer, V. J., and J. A. Day, 1981: A Field Guide to the Atmosphere. Houghton Mifflin Co., 359 pp.

Schultz, D. M., K. M. Kanak, J. M. Straka, R. J. Trapp, B. A. Gordon, D. S., Zrnic , G. H. Bryan, A. J. Durant, T. J. Garrett, P. M. Klein, and D. K. Lilly, 2006: The mysteries of mammatus clouds: Observations and formation mechanisms. In Press at *J. Atmos. Sci.*

Scorer, R., 1972: Clouds of the World: A Complete Color Encyclopedia. Stackpole Books, Harrisburg, PA. 176 pp.

Stith, J. L., 1995: In-situ measurements and observations of cumulonimbus mamma. *Mon. Wea. Rev.*, **123**, 907–914.

Straka, J. M., and J. R. Anderson, 1993: Extension and application of a local, minimum aliasing method to multidimensional problems in limited-area domains. *Mon. Wea. Rev.*, **121**, 2903–2918.

Straka, J. M., and E. R. Mansell, 2005: A bulk microphysics parameterization with multiple ice precipitation categories. *J. Appl. Meteor.*, **44**, 445-466.

Tremback, C. J., J. Powell, W. R. Cotton, and R. A. Pielke, 1987: The forward-in-time upstream advection scheme: Extension to higher orders. *Mon. Wea. Rev.*, **115**, 540-555.

Wagner, F., 1948: Mammatusform als Anzeichen Absinkbewegung in Wolkluft. *Ann. Meteor.*, **1**, 336.

Wang, L. and K. Sassen. 2006: Cirrus mammatus properties derived from an extended remote sensing dataset. *J. Atmos. Sci.* ,63 712–725.

Warner, C., 1973: Measurements of mamma. *Weather*, **28**, 394–397.

Winstead, N. S., J. Verlinde, S. T. Arthur, F. Jaskiewicz, M. Jensen, N. Miles, D. Nicosia, 2001: High-resolution airborne radar observations of mammatus. *Mon. Wea. Rev.*, **129**, 159–166.